Averaged large-signal model of a DC-DC isolated forward resonant reset converter for a solar cell battery charger using internet of things: implementation

Suriyotai Supanyapong[1], Wachiravit Pattarapongsathit[1], Anusak Bilsalam[1,3], Damien Guilbert[2], Phatiphat Thounthong[3]

[1]Department of Electrical Engineering Technology, College of Industrial Technology,
King Mongkut's University of Technology North Bangkok, Bangkok, Thailand
[2]Group of Research in Electrical Engineering of Nancy (GREEN) Laboratory, Université de Lorraine, Lorraine, France
[3]Renewable Energy Research Centre, Department of Teacher Training in Electrical Engineering, Faculty of Technical Education,
King Mongkut's University of Technology North Bangkok, Bangkok, Thailand

Article Info

ABSTRACT

In this study, an analysis and modeling circuit for controlling battery charge solar cells based on data management through internet of things (IoT) is presented. For this proposed, a DC-DC forward resonant reset converter is employed and can be charged at a constant current and constant voltage. Data management of various parameters using IoT technology is provided, via which notifications can be sent to an external application. The proposed converter can give an output voltage of 14.4 V_{DC} for a voltage range including between 9 and 18 V_{DC}, using an isolated transformer and a half-wave rectifier circuit. The main switch of the forward resonant reset converter can operate under a zero-turn-on condition. This approach has the benefit of utilizing a leaking inductance. L_{lkp} and resonant capacitor C_r to reset the remaining flux saturation on the high-frequency transformer. A simulation model prototype was created and tested at a set switching frequency of 50 kHz, 14.4 V_{DC} constant output voltage, and output power of approximately 29 W. An efficiency of 96% at maximum full load can be reached. The proposed analysis techniques and mathematical model were verified via simulation and experimental results, and the obtained results are in agreement with the theoretical analysis.

Corresponding Author:

Suriyotai Supanyapong
Department of Electrical Engineering Technology, College of Industrial Technology
King Mongkut's University of Technology North Bangkok
1518 Pracharat 1 Road, Wongsawang, Bangsue, Bangkok 10800, Thailand
Email: suriyotai.s@cit.kmutnb.ac.th

1. INTRODUCTION

In recent years, high-efficiency and DC-DC converters have been investigated as power sources for distributed photovoltaic cells. In the renewable energy standalone, grid-tie, hybrid, and large and very small ac/dc microgrid systems until the battery charge is applied. Low-voltage power sources, high-efficiency, high-power-density circuits, and regulated outputs are desired for such applications [1]-[3]. Converter topologies are classified into operation pulse-width modulation and semi/full resonant modes. Pulse-width modulation is a basic technique and is subject to the issues of high loss, low efficiency of the main power state during switching, and high electromagnetic interference. To increase the efficiency, the density with the smaller compact size can be editable major is operation semi/full resonant modes, since the current and voltage are out

of phase [4]-[6]. In practical scenarios, a control resonant converter can be used to move the resonant point by changing the input/output voltage or load on the output side. However, the output voltage is not regulated [7]-[9]. The main objective depends on emphasis in the analysis and many parameters on distributed systems, such as voltage, current, power, or observer, each state element. Control methods are classified as linear and nonlinear. Non-linear control has been widely used in complex systems, and controllable state observers are used to realizing good precision and response at the incomprehensive characteristic identity parameter of the plane. High-performance microprocessors are desired for calculating the multi-variable states or most sequence process results and eliminates their drawbacks [10]-[14]. State-of-the-art converters in non-linear system analysis require complex techniques and expertise to realize simple and efficient designs. In some solutions, any method is transformed into a linear system. Generally, averaged model methods (AMMs) are used to estimate the significance of the element variable parameter in a circuit accurately. This is because they are easy to control, accurate, and suitable for use in converters [15]-[18]. AMMs are also used in conjunction with state-space averaging (SSA) in metrology to describe conversion functionality using a general technique with a mathematical model. The small-signal technique, a part of the AMM method, employs investigation impedance-based stability, which provides stability and reliability for the evaluation of converters. It has been applied to single-end and multi-switches comprised of several passive components realizing, extremely accurate analysis results. Decreased discrepancies occur commonly, and the signal flow graph technique method is employed to easily analyze high orders with accuracy [19]-[22]. The large signal technique has been widely used because it is easy to find mathematical models by selectively including and neglecting impedance-based stability analysis. These circuits are mostly used in single-or multi-switch DC converter applications, such as fly-back, forward, and push-pull circuits, and consist of isolated high-frequency transformers, fast recovery diodes, inductors, and capacitors to simplify circuit analysis. In addition, bode plots are used for controller design and mathematical modeling suitable for the analysis of time-variant systems. This approach is fast, easy, accurate, and corresponds to the switching model used [23]-[25]. The concept communication protocol for the internet of things (IoT) to each power unit is depicted in Figure 1. The benefit of IoT platforms are attracting interest from academia and industry because they provide the most practical option for extending the service life of IoT devices when tiny energy sources like thin film batteries, solar cells, and thermoelectric generators are restricted.

　　　　　The remainder of the manuscript is organized as follows. The performance analysis and design of the proposed circuit is discussed in section 2. Section 3 presents the simulation results; experimental results are described in section 4 and finally, section 5 concludes with a section on future work.
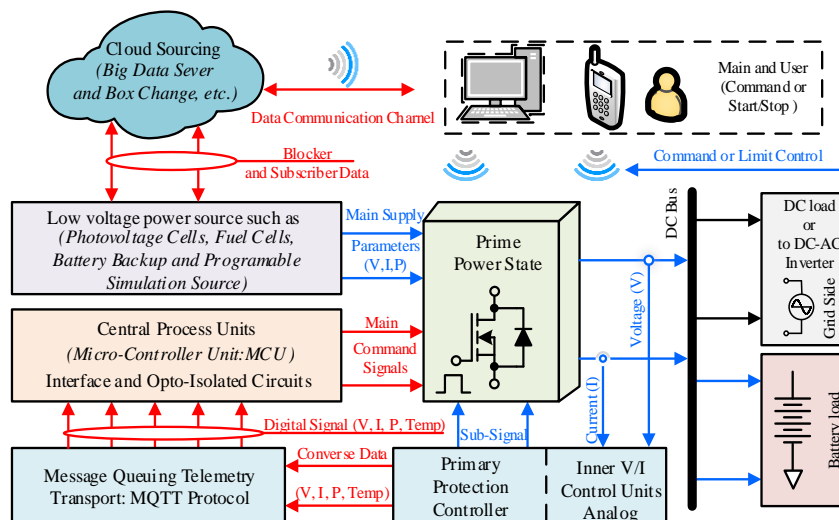

Figure 1. Concept communication protocol for the IoT to each power unit

2. PERFORMANCE PROPOSED CIRCUIT'S ANALYSIS AND DESIGN

2.1. Circuit description

　　　　　The proposed analysis is an averaged large-signal (A-LS) model method of DC-DC isolated forward resonant reset converter (FR-RC) based on a solar cell battery charger for IoT applications, as shown in Figures 2(a)-(f). The power MOSFET M_1 denotes the main switch, C_r is the resonant reset capacitor, and the

high-frequency transformer consists of two windings L_p and L_s, the sum of the magnetizing and leakage inductances are denoted as L_m and L_{lkp}, respectively, built-in primary winding. The leakage inductance secondary side has a lower value and can be ignored. In both components, N_p and N_s are the number of windings in the primary and secondary high frequencies, respectively. D_1, D_2, and L_x denote the converter outputs and current choke inductor, respectively, C_o is the output large capacitor, V_{in} and V_{out} represent the input and output voltages, respectively, and R_o is the battery load. DC-DC isolated forward resonant reset converters convert DC to AC in three stages (inversion: state 1), ac/dc (reset and rectification: state 2), and ac/dc (release energy rectification) and key waveform as shown Figure 2(e).
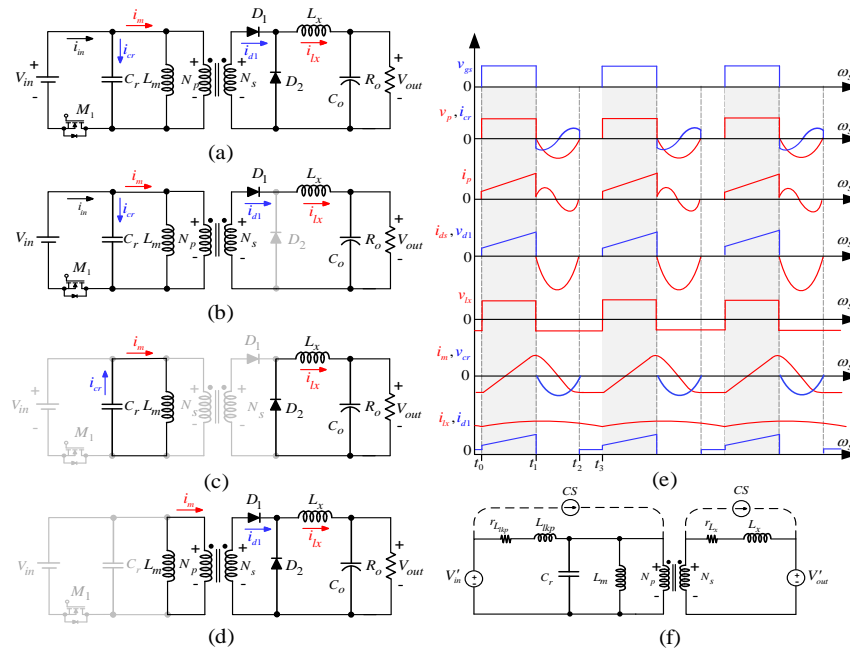

Figure 2. Proposed DC-DC converter system, (a) proposed DC-DC isolated forward resonant reset converter, (b) operation mode of state 1, (c) operation mode of state 2, (d) operation mode of state 3, (e) key waveform of the DC–DC converter, and (f) simplified equivalence circuit of mathematical modeling

2.2. Circuit operation

In state 1, the MOSFET is turned on when the switch M_1 is turned on and operated under the zero turn-on condition, and current flows from the input voltage source V_{in} to the dot terminal of the high-frequency transformer and drain–source. Then, the energy of the primary winding is transferred to the secondary side, and the diode D_1 is turned on by the flow of currents i_{D1} and i_{lx} through the choke inductor and capacitor output, as shown in Figure 2(b). The voltage across the primary and secondary sides can be expressed as (1).

$$V_S(t_{on}) = V_P(t_{on})\left(\frac{N_S}{N_P}\right) = V_{in}\left(\frac{N_S}{N_P}\right) \tag{1}$$

Then, diode D_1 is turned on, while diode D_2 turns off. Therefore, the relationship between the applied voltage and output voltage can be obtained from the slope of the current through the choke output inductor as:

$$v_{Lx} = L_x\frac{di_{Lx}}{dt} = V_{in}\left(\frac{N_S}{N_P}\right) - V_{out} \tag{2}$$

$$\Delta i_{Lx} = \left(V_{in}\left(\frac{N_S}{N_P}\right) - V_{out}\right)\frac{DT_s}{L_x} \tag{3}$$

In state 2, the power switch MOSFET is turned off at the beginning, as shown in Figure 2(c). Then, the magnetizing inductance L_m releases the energy and commutation energy reset flux saturation between L_m and the reset capacitance C_r on the high-frequency transformer. At time t_1-t_2, the waveform reset is approximately two thirds of the half-period switching time T_s, and is observed as a sinusoidal waveform. Then, the diode D_2 turns on, and the output inductor L_x releases energy to the output capacitor C_o from the choke. The ratio of the feed voltage to resistance load R_o can be obtained by (4).

$$\Delta i_{Lx} = -\frac{V_o(1-D)T_s}{L_x} \tag{4}$$

In state 3, the reset capacitance C_r contains the full energy received from the flow back of the current magnetizing inductance L_m from time t_1-t_2. During this time, diodes D_1 and D_2 remain on continuously throughout all components in the output DC side (L_x, C_o, R_o) as shown in Figure 2 (e). From in (3)-(4), a linearly rising current can be seen on the choke output inductor L_x when the MOSFET is turned on. The currents are given by the relations $i_{M1}=i_{in}=i_r+i_m+i_p$ and $i_{Co}=i_{Lx}+i_o$. According to the three-operation state, the conversion ratio M_{DC}, maximum-minimum current on the choke output inductor I_{Lx-max}, I_{Lx-min}, respectively, minimizing choke output inductor L_x, and ripple factor ratio output capacitor C_o can be expressed as (5)-(7).

$$M_{DC} = D\eta \tag{5}$$

$$I_{Lx-\max} = V_o\left(\frac{1}{R} + \frac{1-D}{2L_x f_s}\right); \quad I_{Lx-\min} = V_{out}\left(\frac{1}{R} - \frac{1-D}{2L_x f_s}\right) \tag{6}$$

$$L_{x-\min} = \frac{(1-D)R_o}{2f_s} \tag{7}$$

2.3. Analysis in the operation reset resonant region

In state 2, the power switch MOSFET is turned off. However, the current magnetizing inductance L_m releases energy before the completion time with the protection flux saturation on the high-frequency transformer. By applying the sub analysis resonant mode, the amplitude current magnetizing inductance $i_m = i_r$ is obtained, and the voltage across the reset capacitance is given by $v_{cr}= v_p = v_m$, where v_p and v_m are the voltages across the primary side and magnetizing inductance, respectively. Therefore, the significant parameters are the capacitive reactance of the reset capacitance $X_{Cr}=1/j(2\pi f_r C_r)$ and inductive reactance of the magnetizing inductance $X_{Lm}=j2\pi f_r L_m$. It can be claimed that $X_{Cr}=X_{Lm}$, and the following can be derived.

$$\Delta T_r = \pi\sqrt{L_m C_r} \tag{8}$$

It can be seen that at time t_0-t_1, a square wave form is obtained, in which the amplitude is equal to the input voltage. Moreover, time t_1-t_2 can occur in the reset sinusoidal waveform. At time t_2-t_3 can be neglected because of the non-wave form. Hence, the amplitude reset voltage V_{Cr} can be derived as:

$$\int_0^{DT_{sw}} V_{in}dt + \int_{DT_{sw}}^{D_r T_{sw}} V_p \sin\left(\frac{\pi}{2} + 2\pi f_r t\right)dt = 0 \tag{9}$$

$$V_{in}(DT_{sw}) + \frac{V_p}{\omega_r}\left(\cos(\omega_r D_r T_{sw}) - \cos(\omega_r DT_{sw})\right) = 0 \tag{10}$$

Where is the interval time of the angle reset resonant time $\omega r DT_{sw} = \pi$, the surface time approximates nearly $\omega_r D_r T_{sw}\, 2\pi$, and the angular of a resonant frequency $\omega_r = 1/squ\,(L_m C_r)$ can be obtained by (11):

$$V_{in}(DT_{sw}) + 2V_p\sqrt{L_m C_r} = 0 \tag{11}$$

Simplifying in (11), the final result is expressed (12), and last step is simplified equivalence circuit of mathematical modeling as shown in Figure 2(f):

$$V_p = -\frac{\pi V_{in} D f_r}{f_s} \tag{12}$$

2.4. Mathematical A-LS modeling

Since DC-DC isolated forward resonant reset converters convert DC to AC in three stages, a mathematical A-LS analysis model has the following state variables: $[i_{lm}, i_{lx}, v_{cr}, v_{out}]$. The precision of the modeling can be improved by including the leakage inductance L_{lkp} and parasitic resistance r_{Lx} of the choke output inductor L_x. By applying Kirchhoff's voltage and current laws to the input and output power converter circuit depicted in Figure 2(f), the following differential equations in three completed descriptions of the power stage are derived as (13a) to (14b):

State 1: input side (where $v_{in}=v_p$, $v_{rlke}=r_{lke}$, $i_{lke}=i_{rlke}$)

$$-v_{in} + v_{lke} + v_{rlke} + v_{lm} + v_{cr} = 0 \tag{13a}$$

$$i'_{lm} = \frac{-v_{cr} - v_{lke} - r_{lke}i_{lke} + v_{in}}{L_m} \tag{13b}$$

$$i_{cr} = -i_{lke} \tag{14a}$$

$$v'_{cr} = \frac{-i_{lke}}{C_r} \tag{14b}$$

The state variable current choke inductor i'_{lx} and voltage across capacitor v'_{co} at the output DC side can be obtained as:

$$-v_s + v_{Lx} + v_{co} + v_{rlx} = 0 \tag{15a}$$

$$i'_{lx} = \frac{nv_{in} - v_{co} - r_{lx}i_{lx}}{L_x} \tag{15b}$$

$$i_{lx} = i_{ro} + i_{co} \tag{16a}$$

$$v'_{co} = \frac{1}{C_o}\left(ai_{Lm} - \frac{v_{co}}{R_o}\right) \tag{16b}$$

By multiplying the symmetry state variable in both operations, the similarity of states 2 and 3 can be derived as (17)-(20). Hence, the differential equations in state 2 are expressed as:

$$i'_{lm} = \frac{-v_{cr}}{L_m} - \frac{r_{Llkp}i_m}{L_m} \tag{17}$$

$$v'_{cr} = \frac{i_{lm}}{C_r} \tag{18}$$

$$i'_{Lx} = \frac{-v_{cr} - r_{Llkp}i_{lx}}{L_x} \tag{19}$$

$$v'_{co} = \frac{1}{C_o}\left(i_{Lx} - \frac{v_{co}}{R_o}\right) \tag{20}$$

In state 3, the current circulating through the magnetizing inductance L_m and primary winding N_p can be written as:

$$i'_{lm} = \frac{v_p}{L_m} \tag{21}$$

By applying Kirchhoff's voltage law, the state variable voltage across the choke output inductor v_{lx} and voltage capacitor at the DC output depending on the real current direction, the obtained stage 2 loops can be separated as:

$$v_{lx} = v_{in} - v_{rlx} - v_{co} \tag{22a}$$

$$v_{co} = -v_{rLx} - v_{Lx} \tag{22b}$$

In the (22a) is substituted into (22b) to obtain

$$v_s = 0 \tag{23}$$

The end differential equations for the state variable of the voltage capacitor output can be expressed as:

$$v'_{co} = \frac{1}{C_o}\left(ai_{Lm} - \frac{v_{co}}{R_o}\right) \tag{24}$$

From this differential equation, state 1 can be used in (13b), (14b), and (15b) and (16b), state 2 can be used in (17)-(20), and state 3 can be used in (21), (23), and (24). The three-state operation of the state variable parameters is rewritten as the general form of SSA expressed as:

$$\overset{\bullet}{x} = Ax + Bu \tag{25}$$

Therefore, in the average system solution, we have the combined subsystems A1, A2, A3, and sub-inputs B1, B2, and B3. where, are (*d*) and (1-*d*) during time power switch turn on (*d*) in state 1 and turn off (1-*d*) time in both two and three states, and the combinate parameters are expressed as:

$$A = A_1 + A_2 + A_3 = \begin{bmatrix} -\dfrac{r_{lke}}{L_m} & 0 & -\dfrac{1}{L_m} & 0 \\[2mm] \dfrac{-r_{lx}}{L_x} & 0 & 0 & -\dfrac{1}{L_x} \\[2mm] 0 & 0 & 0 & 0 \\[2mm] \dfrac{a}{C_o} & 0 & 0 & -\dfrac{1}{C_o R_o} \end{bmatrix}(d) + \begin{bmatrix} -\dfrac{r_{lke}}{L_m} & 0 & -\dfrac{1}{L_m} & 0 \\[2mm] -\dfrac{r_{lx}}{L_x} & 0 & 0 & -\dfrac{1}{L_x} \\[2mm] \dfrac{1}{C_r} & 0 & 0 & 0 \\[2mm] 0 & \dfrac{1}{C_o} & 0 & -\dfrac{1}{C_o R_o} \end{bmatrix}(1-d)$$

$$+ \begin{bmatrix} 0 & 0 & 0 & 0 \\ 0 & 0 & 0 & 0 \\ 0 & 0 & 0 & 0 \\ \dfrac{a}{C_o} & 0 & 0 & -\dfrac{1}{C_o R_o} \end{bmatrix}(1-d) \tag{26}$$

$$B = B_1 + B_2 + B_3 = \begin{bmatrix} \dfrac{1}{L_m} \\[2mm] \dfrac{n}{L_x} \\[2mm] 0 \\[2mm] 0 \end{bmatrix}(d) + \begin{bmatrix} 0 \\ 0 \\ 0 \\ 0 \end{bmatrix}(1-d) + \begin{bmatrix} 0 \\ 0 \\ 0 \\ 0 \end{bmatrix}(1-d) \tag{27}$$

Simplifying of a (26) and (27), the relationship between the state variables can be written as:

$$x' = \begin{bmatrix} i'_{lm} \\ i'_{lx} \\ v'_{cr} \\ v'_{co} \end{bmatrix} = \begin{bmatrix} -\dfrac{r_{lke}}{L_m} & 0 & -\dfrac{1}{L_m} & 0 \\ -\dfrac{r_{lx}}{L_x} & 0 & 0 & -\dfrac{1}{L_x} \\ \dfrac{1-d}{C_r} & 0 & 0 & 0 \\ \dfrac{a}{C_o} & \dfrac{1-d}{C_o} & 0 & \dfrac{d-2}{C_o R_o} \end{bmatrix} \begin{bmatrix} i_{lm} \\ i_{lx} \\ v_{cr} \\ v_{co} \end{bmatrix} + \begin{bmatrix} \dfrac{d}{L_m} \\ \dfrac{nd}{L_x} \\ 0 \\ 0 \end{bmatrix} [v_{in}] \tag{28}$$

2.5. Communication of the internet of thing unit

The IoT was divided into two parts. The first part involves the receive for measured using data communication of the voltage, current, and temperature output into the microcontroller unit. In the first step, the point ground between the measured voltage input power state and the analog to digital part (ADCs) unit sends data until the MCU because of the divergent ground type. The isolated unit has a function-separated power and control circuit, and it can provide good protection read data and measured value parameters. In the measured voltage divider 3.3 V_{DC} from the DC voltage charge output 14.4 V_{DC} at the full power design. The second part involves the receive-send of IoT until the MQTT protocol is provided into the machine-to-machine part, as illustrated in Figure 3, the equipment-to-equipment support consists of publishers, brokers, and subscribers. The publisher will function the sent data, and measure the value information (DC-DC converter, battery). The broker will be the function intermediary management that converts the difference signal (ADC, DAC), and the subscriber will be the function data reference or algorithm sequence.
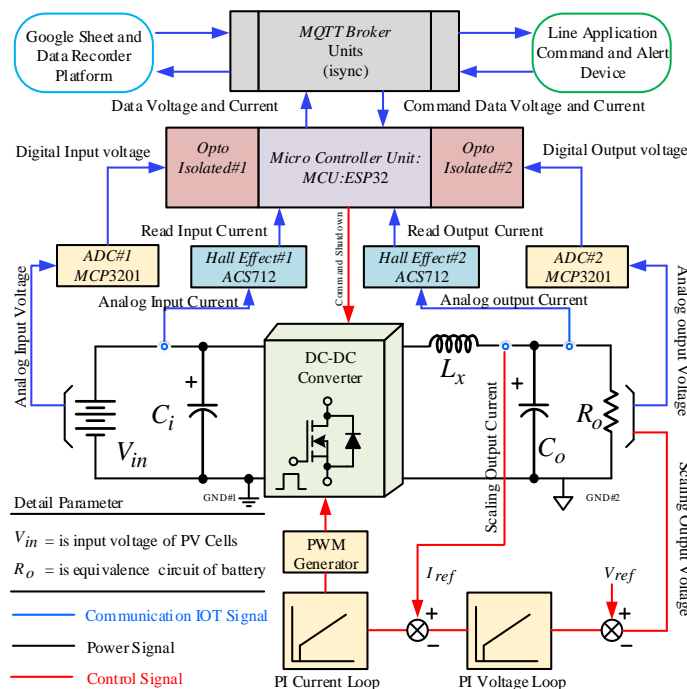

Figure 3. Proposed communication between IoT and the DC-DC converter system

2.6. Power state design

The operation of the proposed converter in the CCM is illustrated in Figure 2(a). In the steady-state operation, the circuit is designed (29)–(39) to be operated at a 50 kHz fixed switching frequency, approximate wide input voltage 9–19 V_{DC}, current 2.16 A, frequency transformer with ferrite core (PQ 25/19/26/25 N87), and four primary winding turns. Therefore, the number of secondary windings N_s is given by:

$$N_s = \frac{N_p V_{out}}{V_{in} D} = \frac{4 \times 14.4}{16 \times 0.4} = 9 \, \text{Turns} \tag{29}$$

The voltage stress on the switches can be obtain by:

$$V_{DS-\max} = V_{in} - V_p \tag{30}$$

Here, the maximum duty cycle is $D_{max}=1-(\Delta T_R - T_s)$. By substituting the peak primary winding in (12) into (30), the voltage stress on the switches is expressed as:

$$V_{DS-\max} = V_{in} - \left(\frac{V_{in} D_{\max} T_s}{2\sqrt{L_m C_r}} \right) = 16 + \frac{16 \times 0.6 \times 20 \times 10^{-6}}{2\sqrt{80 \times 10^{-6} \times 81.056 \times 10^{-9}}} = 53.699 \, \text{V} \tag{31}$$

The maximum current in the DC input side can be expressed as:

$$I_{in-\max} = \frac{N_s}{N_p} \times V_{out} \left(\frac{1}{R_o} + \frac{(1-D)}{2L_x f_s} \right) = 32.4 + \left(\frac{1}{7.2} + \frac{(1-0.4)}{2 \times 216 \times 10^{-6} \times 50 \times 10^3} \right) = 5.4 \, \text{A} \tag{32}$$

After the design is a parameter of the voltage stress, and the average currents of the fast recovery diode $V_{D1\text{-}max}$, $I_{D1\text{-}max}$, can be derived as:

$$V_{D1-\max} = \frac{N_s}{N_p} \times \left(\frac{V_{in} D_{\max} T_s}{\sqrt{L_m C_r}} \right) = 2.25 \times \frac{16 \times 0.6 \times 20 \times 10^{-6}}{\sqrt{80 \times 10^{-6} \times 81.056 \times 10^{-9}}} = 169.647 \, \text{V} \tag{33}$$

$$I_{D1-\max} = I_{Lx-\max} = V_{out} \times \left(\frac{1}{R_o} + \frac{1-D}{2L_x f_s} \right) = 14.4 \times \left(\frac{1}{7.2} + \frac{1-0.4}{2 \times 216 \times 10^{-6} \times 50 \times 10^3} \right) = 2.4 \, \text{A} \tag{34}$$

Finally, the designed active component is the voltage stress, and the average currents of the fast recovery diodes $V_{D2\text{-}max}$, and $I_{D2\text{-}max}$ can be calculated as:

$$V_{D2-\max} = \left(\frac{N_s}{N_p} \right) V_{in} = \left(\frac{9}{4} \right) \times 16 = 36 \, \text{V} \tag{35}$$

According to (29), if the turn ratio is $a=2.25$, the measured magnetizing inductance from the LCR meter is designed to be 80 µH, the duty cycle is approximately 0.4. Then, it can be found that the reset resonant capacitor provides the reset setting time $\Delta T_r = 0.4 \, Ts$, and can be calculated as:

$$C_r = \left(\frac{\Delta T_r}{\pi} \right)^2 \times \frac{1}{L_m} = \left(\frac{0.4 \times 20 \times 10^{-6}}{\pi} \right) \times \frac{1}{80 \times 10^{-6}} = 81.056 \, \text{nF} \tag{36}$$

To minimize the choke output inductor $L_{x\text{-}min}$ on the DC output side

$$L_{x-\min} = \frac{(1-D)R_o}{2f_s} = \frac{(1-D) \times 7.2}{2 \times 50 \times 10^3} = 43.2 \, \mu\text{H} \tag{37}$$

Consequently, to ensure that the characteristics of the proposed circuit meet the above analysis, the proposed circuit needs to be operated in CCM. Then, by increasing the inductance of the choke output inductor, the inductor design value can be obtained as:

$$L_{x-CCM} = 5L_{x-\min} = 5 \times 43.2 \times 10^{-6} = 216 \, \mu\text{H} \tag{38}$$

The value of the output capacitance C_o depends mainly on the ripple output voltage factor V_{rip}. Assuming $\Delta V_{out}/V_{out}$ to be less than 1%, this can be calculated as:

$$C_o = \frac{(1-D)}{8L_x(f_s)^2} \times \frac{V_{out}}{\Delta V_{out}} = \frac{(1-0.4)\times 7.2}{8 \times 216 \times 10^{-6}(50\times 10^3)^2} \times \frac{14.4}{0.01} = 200\,\mu F \tag{39}$$

Finally, in the implementation, the output capacitance was chosen as C_o=330 μF/50 V. A overall relationships of the parameter of the proposed circuit from calculation as shown in Figures 4(a)-(c).
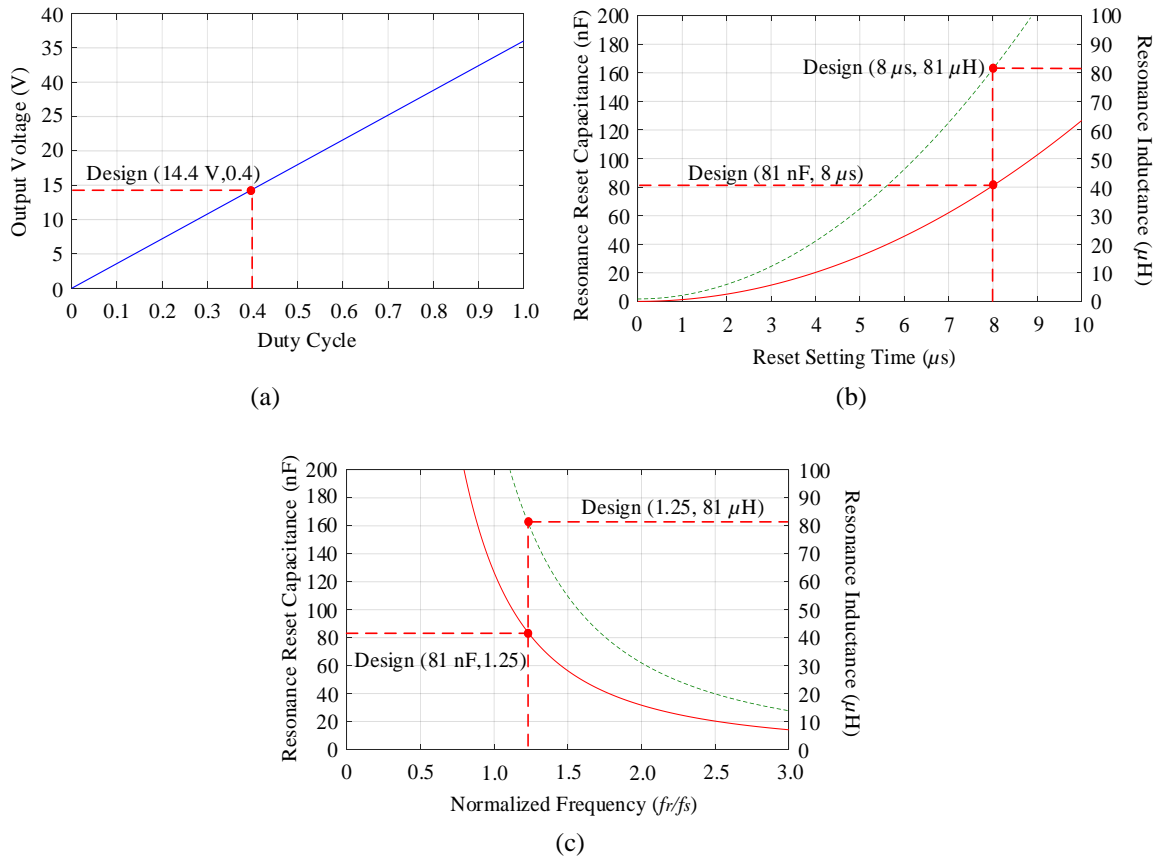

(a)   (b)

(c)

Figure 4. Relationships of the parameter of the proposed circuit: (a) normalized output versus varying duty cycle, (b) relationship between reset resonance capacitance and reset setting time and resonance inductance, and (c) relationship between reset resonance capacitance and normalized frequency and resonance inductance

3.   SIMULATION RESULTS

A prototype of the proposed circuit was simulated using a mathematical model with the parameters listed in appendix. In this section, the state variable of an A-LS method of a DC-DC isolated forward resonant reset converter based on a solar cell battery charger response is discussed. The configuration of the proposed technique was a simulated mathematical model with the SIMULINK program. The purpose of this simulation is to verify the analysis methods and study the static state variable and dynamic performance of the system. The converter under consideration is capable of: 1) correctly predicting the state variable [i'_{lm}, i'_{lx}, v'_{cr}, v'_{out}] waveforms by using the A-LS model 2) obtaining the dynamic response of the output voltage charger. A rated operation is considered at 14.4 V_{DC}, 2 A are shown Figures 5(a) and 5(b), and approximately 29 W output power at full-load condition. The overall static simulation results are shown in Figures 5.

The simulated waveforms of the output voltage v'_o and output current i'_{Lx} waveforms were simulated at an output voltage of 14.4 V_{DC} output current of ~2 A, and output power of ~29 W. The waveforms in Figures 6(a) and 6(b) show the results of the state variable of the current magnetizing inductance, and it can be seen that the sinusoidal waveforms are similar. The voltage across the reset resonance, which was operated under resent to achieve the reset of the remaining flux saturation on the high-frequency transformer is shown in Figures 7(a) and 7(b).
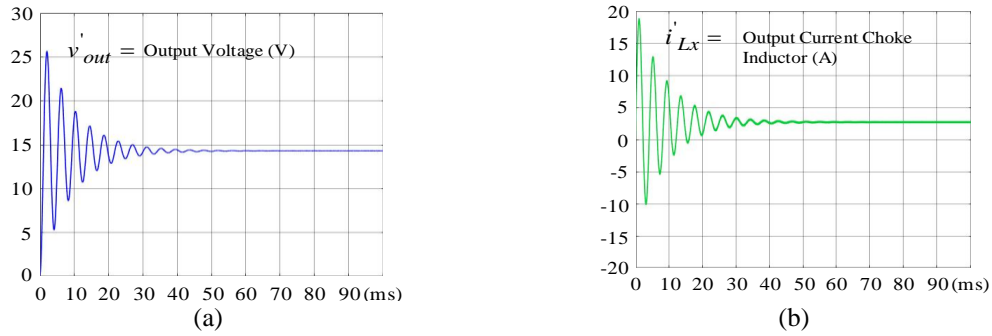
Figure 5. Simulation results for state variables of (a) output voltage v'_{out} and (b) output current i'_{Lx} waveform
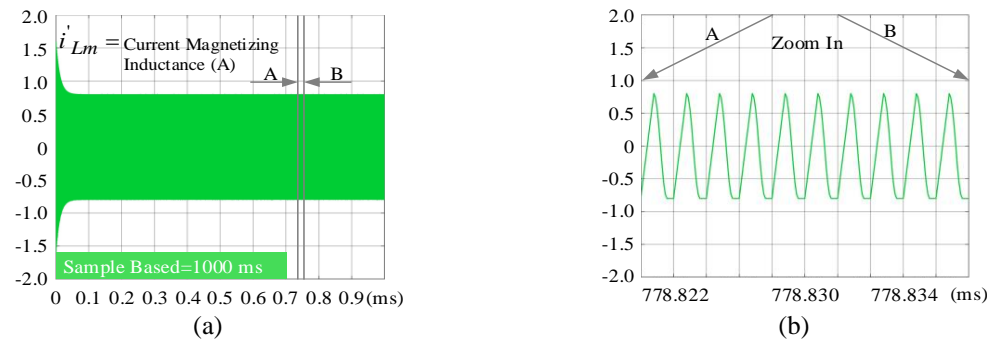

Figure 6. Simulation results for the state variable of the current magnetizing inductance (a) transient time and (b) zoomed in waveform
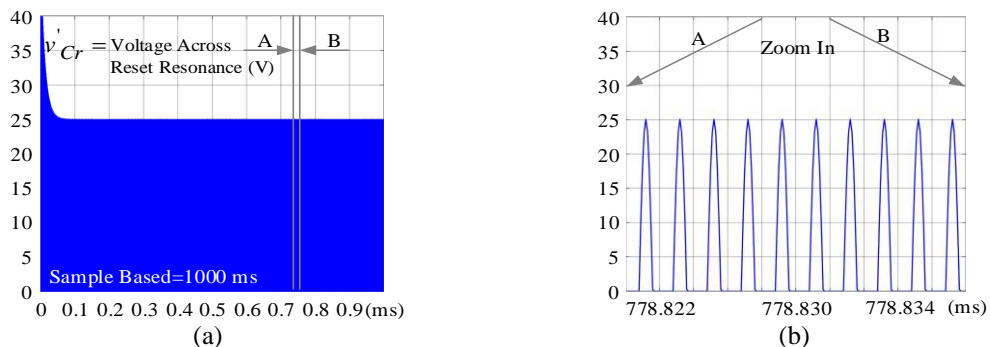

Figure 7. Simulation results of the state variable of the voltage across reset resonance (a) transient time and (b) zoomed in waveform

The simulation analyzes the result model and load conditions at 0.2–0.325 s: constant operated at load and 0.325–0.649 s: based on step load condition and before 0.649 s: return to the first condition. The simulation results of the proposed system are shown in Figures 8(a)-8(f), where the output voltage return to the setpoint is achieved. The first results of the transient response of the output voltage at step load half-load to no-load were overshoot of 14.47 V. Setting the set time point to 24 ms and the return load recovery time to 33 ms resulted in undershoot of 14.35 V, as shown in Figures 8(a) and 8(b). The second results of the transient response of the output voltage at step load full-load to no-load were overshoot 14.49 V, and setting time to setpoint 34 ms and return load recover time to set point is 44 ms resulted in undershoot of 14.37 V, as shown in Figures 8(c) and 8(d). The final results of the transient response of the output voltage at step full-load to half-load were less overshoot of 14.48 V, and setting the time to set point 27 ms and return load recover time to set point 14 ms, the undershoot was less than 14.36 V, as shown in Figures 8(e)-8(f).
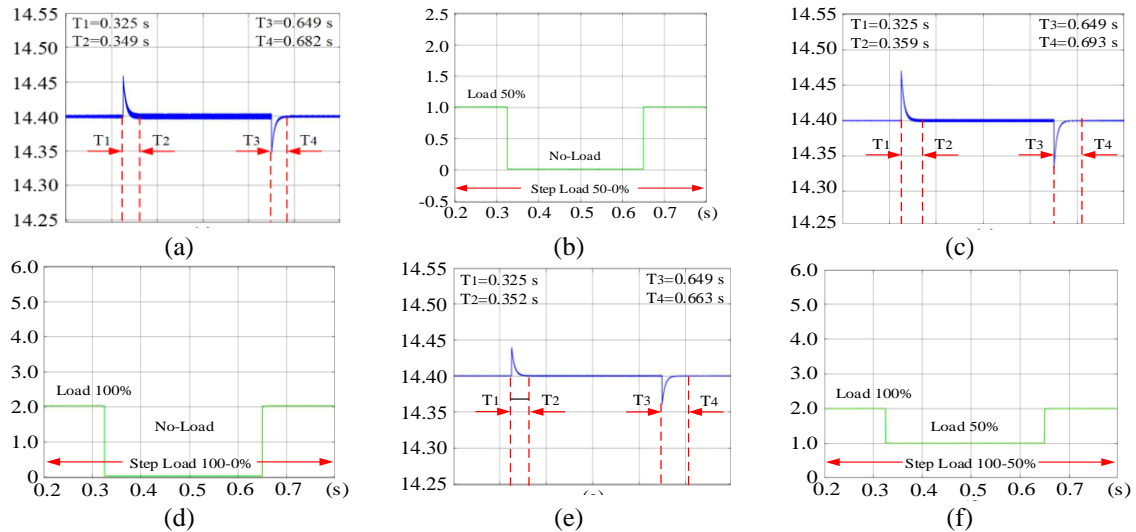
Figure 8. Simulation results of the dynamic response of the output voltage charger: (a)-(b) response voltage and current at step load half-load to no-load, (c)-(d) response voltage and current at step load full-load to no-load condition, and (e)-(f) response voltage and current at step load half-load to full-load condition

4. EXPERIMENTAL RESULTS

4.1. Open loop results

A prototype of the FR-RC was used as a specification parameter for the experimental results, and the circuit parameters listed in appendix were used in the implementation. Figure 9, the photos of the experimental setup are composed of i) DC power supply setup, ii) phototype circuit, iii) oscilloscope display, iv) resistance load setup and then number 5-7 are measurement tool v) differences probe, vi) current probe, vii) digital multimeter and finally equipment number 8 is battery load setup. Most of the experimental results are shown in Figures 10 and 11. The voltage, current, and power waveform at the input side were measured, and the input power was approximately 29 W, as shown in Figure 10(a). Figures 10(b) and 10(c) show the switch voltages and current, and can be seen that the reset time for the remaining flux magnetics of the current reset resonance capacitor. Figure 10(d) shows that the main switch operated under the zero-turn-on condition.
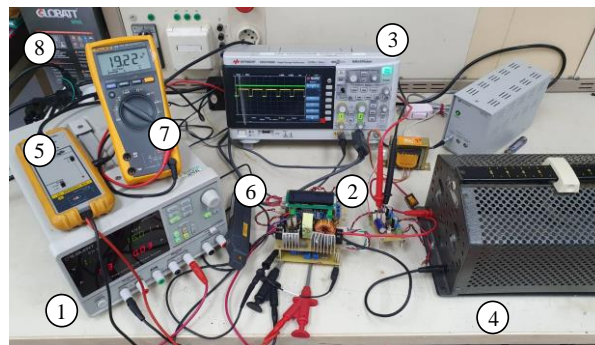

Figure 9. Experimental setup in laboratory for proposed scheme

The voltage waveforms of the high-frequency half quasi-square-wave voltage across the primary v_p and the voltage across the secondary v_s are as shown in Figure 11(a). The waveform of the diode voltage v_{D1}, current i_{D1}, and diodes operated under low-loss conditions are shown in Figure 11(b). The voltage and current of the choke output inductor are the square-wave voltage v_{Lx} and current triangle waveform i_{Lx}, respectively, as shown in Figure 11(c). Finally, the output side waveform for the measured voltage, current, and power at the output side had a maximum value of 29 W, as shown in Figure 11(d).
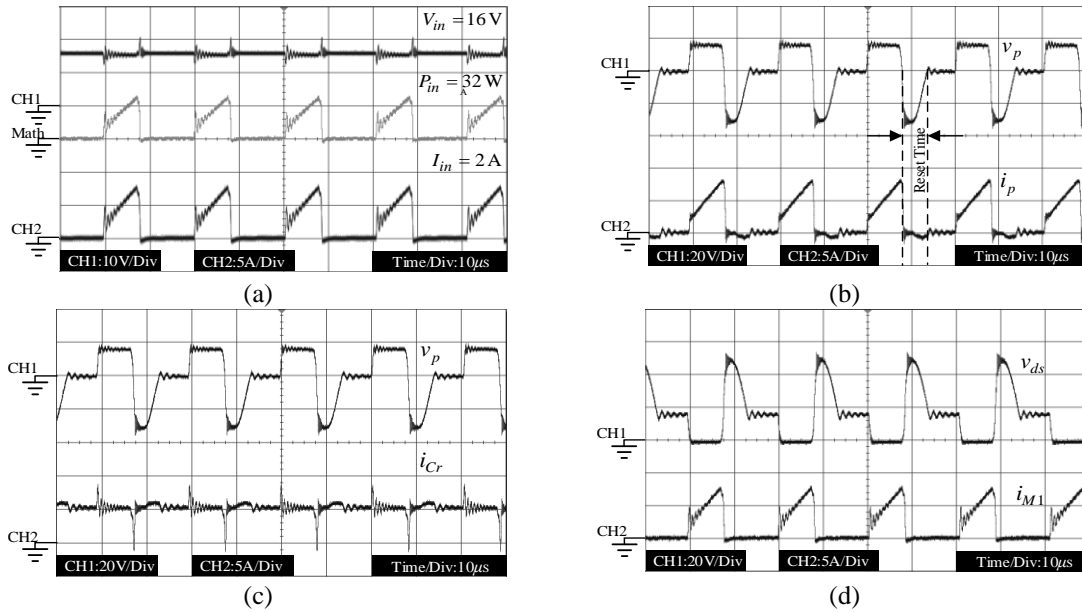
Figure 10. Experimental result of the proposed circuit: (a) measured voltage V_{in}, current I_{in}, and power P_{in} waveforms at the input side; (b) measured voltage across v_p and current i_p at the high frequency transformer; (c) measured voltage across primary winding v_p and current reset resonance i_{Cr}; and (d) measured voltage v_{ds} and current i_{M1} waveforms of the MOSFET switch
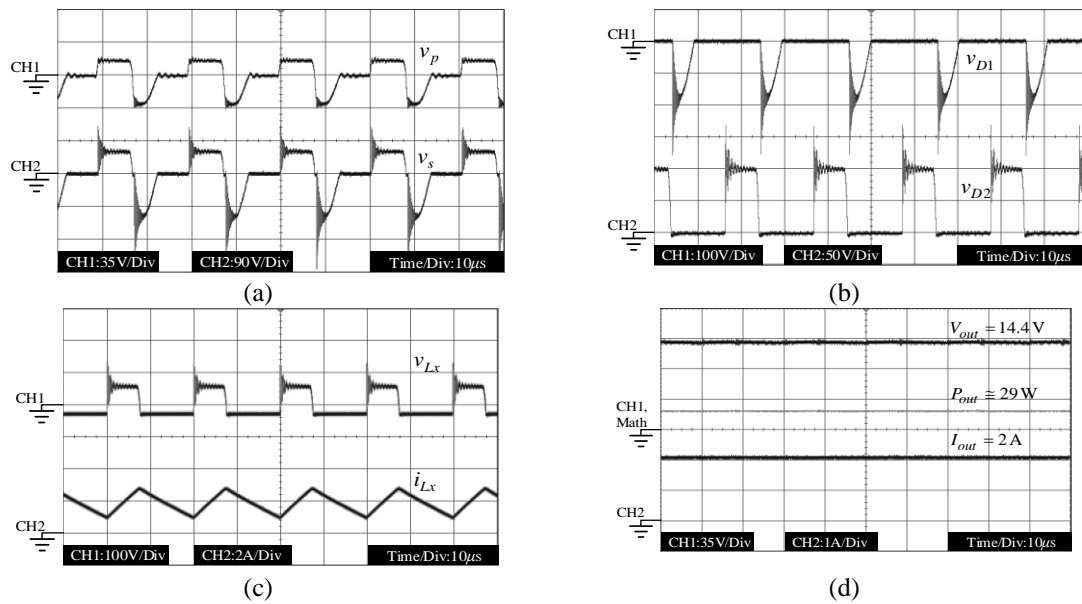

Figure 11. Experimental results of the proposed circuit: (a) measured operated transfer of voltage across primary winding v_p and voltage across secondary winding v_s at the high frequency transformer; (b) measured diode voltage v_{D1} and voltage v_{D2}; (c) measured voltage across v_{Lx} and current i_{Lx} of the choke inductor; and (d) measured voltage V_{out}, current I_{out}, power P_{out} waveforms at the input side

4.2. Close loop results

An FR-RC has been built and measured the parameter static value waveform. The main objective is to control the regulated output voltage of the close-up voltage and current charge battery, as shown in Figures 12 to 14. An auxiliary analog circuit was used in the control units of the prototype. The response of the attentive overshoot and recovery time while changing the load from no-load to half-load and from half-load to no-load based on the return load, the first situation was 5 and 330 ms to set point, and an overshoot 4.167%, are shown in Figures 12(a) and 12(b). In the next step, the current load is increased from no-full load and full-no load, set points were 8 and 500 ms, and overshoot of 4.167% was observed, as shown in

Figures 13(a) and 13(b). In the third situation, minor changes were made from half-load to full-load and from full-load to half-load at 5 and 10 ms set points, and an overshoot of 4.167% was observed, as shown in Figures 14(a) and 14(b) and brief overall response results as shown in Table 1, respectively. However, a low ripple factor is an important problem in the design, associated with the enhanced reverse time resulting from the use of bulk output capacitors. Therefore, the unaffected magnitude of the voltage, current, and performance charge of the battery load. The performance measurements of the proposed circuit are reported in terms of constant voltage and current charge when the input voltage is varied from 9 to 18 V, and the percentage regulation is less than 0.5% in the three situations, as shown in Figure 15(a). The maximum overall efficiency of the proposed circuit was 94% at a low irradiation input level of 9–13 V, while normal irradiation had an input level of 13–18 V, and the measured efficiency was approximately more than 90% throughout the operating period, as shown in Figure 15(b). The experimental prototype is shown in Figure 16 and the experimental test record data charger in excel on the google sheet platform is shown in Figure 17.
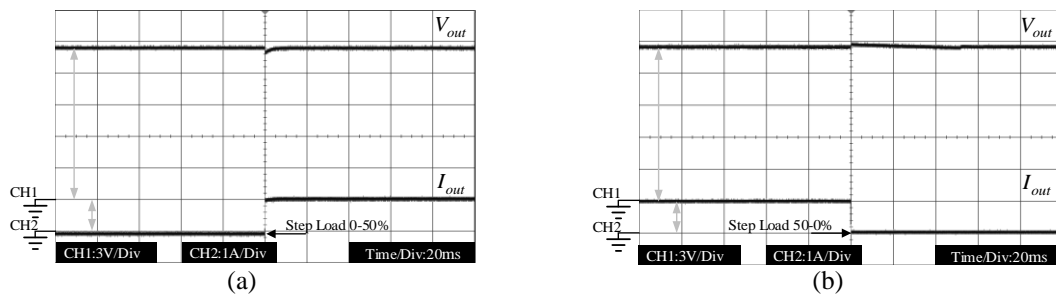

Figure 12. Experimental results of the dynamic response of the output voltage of the charger (a) response voltage at current step load no-load to half-load and (b) response voltage at current step load half-load to no-load condition
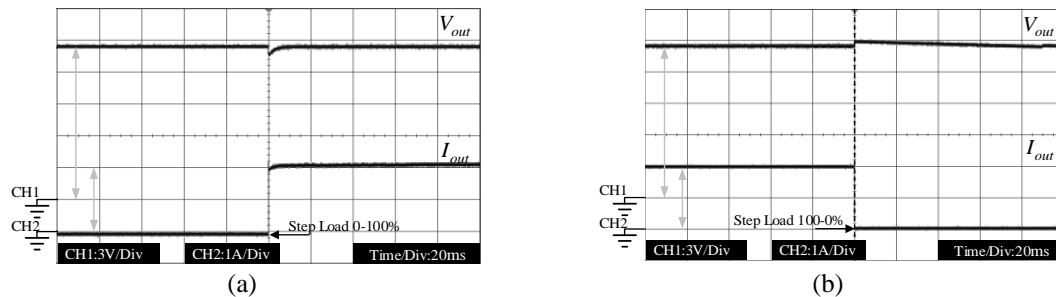

Figure 13. Experimental results of the dynamic response of the output voltage of the charger (a) response voltage at current step load no-load to full-load and (b) response voltage at current step load full-load to no-load condition
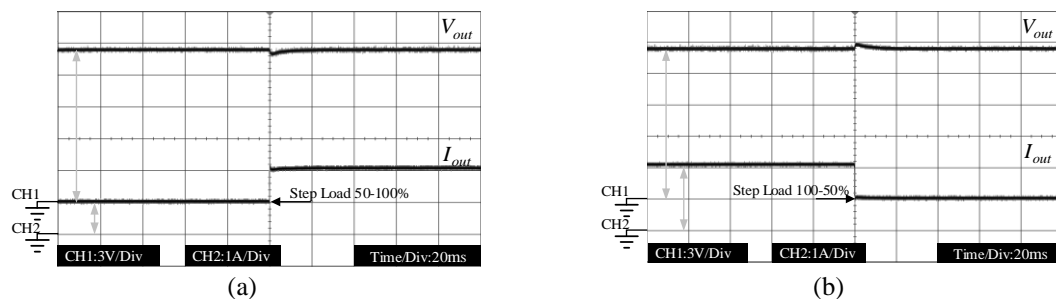

Figure 14. Experimental results of the dynamic response of the output voltage of the charger (a) response voltage at current step load half-load to full-load and (b) response voltage at current step load full-load to half-load condition
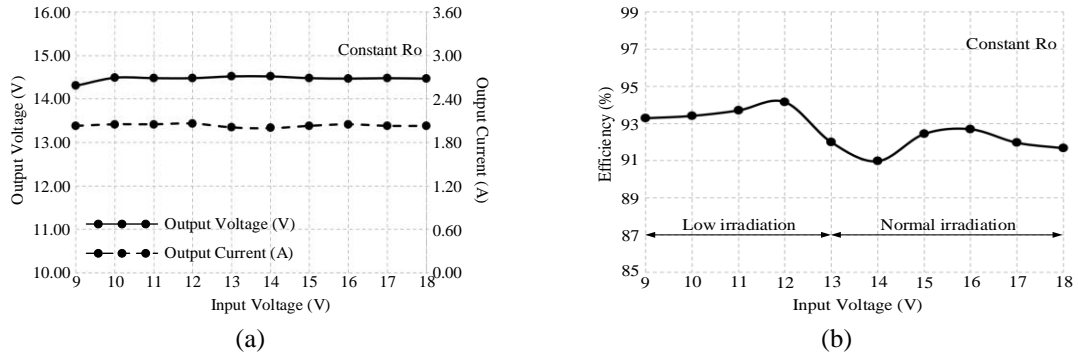
Figure 15. Experimental result of relationship graphs (a) relationship between output voltage V_{out} and varied input voltage V_{in} and output current I_{out} and (b) relationship between efficiency and input voltage V_{out}

Table 1. The performance of proposed circuit

| Condition	Parameters	Simulation results	Experimental results	Remark
I	Under/over shoot	0.347%/0.689%	4.167%/4.167%	No-load to half-load and return condition
	Setting time	33 ms/24 ms	5 ms/330 ms	
	Regulation output voltage	0%/0%	0.186%/0. 186%	
II	Under/over shoot	0.555%/0.394%	4.167%/4.167%	No-load to full-load and return condition.
	Setting time	44 ms/34 ms	8 ms/500 ms	
	Regulation output voltage	0%/0%	0.345%/0.345%	
III	Under/over shoot	0.208%0.48%	4.167%/4.167%	Half-load to full-load and return condition.
	Setting time	14 ms/27 ms	4 ms/10 ms	
	Regulation output voltage	0%/0%	0.158%/0.158%	
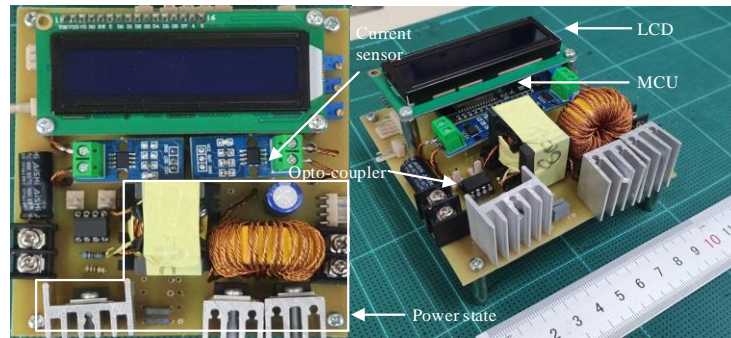
Figure 16. Detail and photograph of the proposed circuits
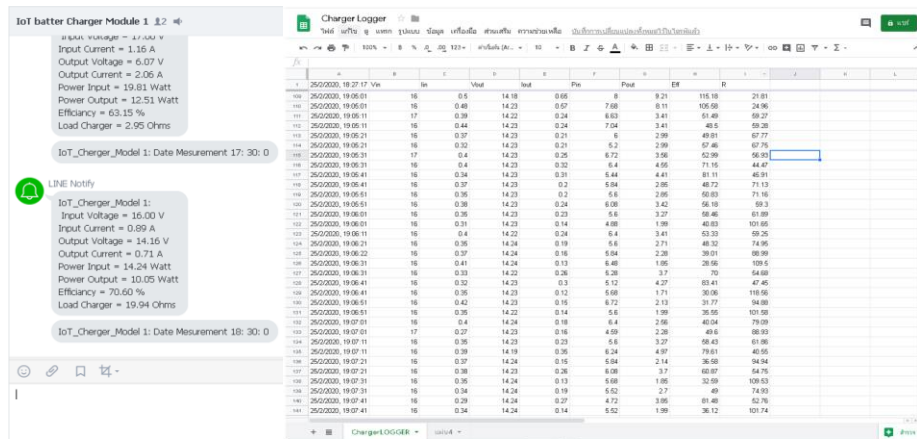

Figure 17. Record data charger in excel on the google sheet platform

5. CONCLUSION AND FUTURE WORK

In this study, circuits for control battery-charged solar cells based on data management through IoT using a DC-DC forward resonant reset converter have been analyzed and modeled. The simulated mathematical model is capable of: 1) obtaining the correct state variable waveform by using an A-LS model; and 2) obtaining the dynamic response of the output voltage charger when changing from 50% to 0%, 100% to 0%, and 100% to 50% level load output. The main advantages of the proposed system are the observation of the state variable for a mathematical model built using an A-LS model of a frond-end DC-DC forward resonant reset converter and controllable main power stages. A basic simple control unit has also been proposed, enabling enhancing the dynamic response. The simulation results confirmed that at a heavy step load change, the desired setting and recovery time to set the point output voltage charge can be obtained based on the assumption of a regulative condition. The experimental results of the proposed system confirmed that at light-load to full-load conditions, low power loss for each component, reset flux saturation on the high-frequency transformer, satisfactory are low overshoot, less time reveres time, great percent regulation output voltage, and can be a good response IoT platform and record data during charging of the battery at all times. Future work will focus on enhancing wireless power transmission by reducing the high frequency transformer while charging series batteries on the battery management system (BMS) using the IoT.

APPENDIX

Input voltage V_{in}=desing16 V_{DC} (wide range 9–18 V_{DC}), output voltage V_{out}=14.4 V_{DC} (regulation range), output current I_{out}=2 A (approximate current charge), number of primary windings N_p=9 turns (L_p=145.623 μH, (AWG#26*3)), number of secondary windings N_s=4 turns (L_s=1.08 mH (AWG#26*2)), reset resonant capacitance C_r=81.056 nF (Polypropylene), output choke inductance L_x=216 μH (ferrite toroid/31/1.3), output capacitance C_o=330 μF (Electrolytic/50 V), power switch MOSFET M=IRFP 3205 (N-Channel MOSFET V_{DSS}=55 V, I_D=110 A, $R_{DS\,(on)}$=8.0 mΩ), fast recovery diode D_1, D_2=MUR1520 (V_{RRM}=200 V, $I_{F(AV)}$=15 A, V_F=0.85 V), gains voltage control unit k_{pv}, k_{iv}=5.867, 3333.33, gains current control unit k_{pi}, k_{ii}=12.712, 18031

REFERENCES

[1] Q. Li and P. Wolfs, "A Review of the Single Phase Photovoltaic Module Integrated Converter Topologies With Three Different DC Link Configurations," *IEEE Transactions on Power Electronics*, vol. 23, no. 3, pp. 1320-1333, May 2008, doi: 10.1109/TPEL.2008.920883.

[2] P. Thounthong, B. Davat, S. Rael and P. Sethakul, "Fuel cell high-power applications," *IEEE Industrial Electronics Magazine*, vol. 3, no. 1, pp. 32-46, 2009, doi: 10.1109/MIE.2008.930365.

[3] W. Li and X. He, "Review of Nonisolated High-Step-Up DC/DC Converters in Photovoltaic Grid-Connected Applications," *IEEE Transactions on Industrial Electronics*, vol. 58, no. 4, pp. 1239-1250, 2011, doi: 10.1109/TIE.2010.2049715.

[4] M. Z. Zulkifli, M. Azri, A. Alias, N. Talib and J. M. Lazi, "Simple control scheme buck-boost DC-DC converter for stand alone PV application system," *International Journal of Power Electronics and Drive System (IJPEDS)*, vol. 10, no. 2, pp. 1090-1101, 2019, doi: 10.11591/ijpeds.v10.i2.pp1090-1101.

[5] M. O. Ali and A. H. Ahmad, "Design, modelling and simulation of controlled sepic DC-DC converter-based genetic algorithm," *International Journal of Power Electronics and Drive System (IJPEDS)*, vol. 11, no. 4, pp. 2116-2125, 2020, doi: 10.11591/ijpeds.v11.i4.pp2116-2125.

[6] A. A. M. Faudzi, S. F. Toha, R. A. Hanifah, N. F. Hasbullah and N. A. Kamisan, "An interleaved DC charging solar system for electric vehicle," *International Journal of Power Electronics and Drive System (IJPEDS)*, vol. 12, no. 4, pp. 2414-2422, 2021, doi: 10.11591/ijpeds.v12.i4.pp2414-2422.

[7] X. Huang, X. Wang, T. Nergaard, J. S. Lai, X. Xu and L. Zhu, "Parasitic ringing and design issues of digitally controlled high power interleaved boost converters," *IEEE Transactions on Power Electronics*, vol. 19, no. 5, pp. 1341-1352, 2004, doi: 10.1109/TPEL.2004.833434.

[8] Q. Zhao and F. C. Lee, "High-efficiency, high step-up DC-DC converters," *IEEE Transactions on Power Electronics*, vol. 18, no. 1, pp. 65-73, 2003, doi: 10.1109/TPEL.2002.807188.

[9] L. Huber and M. M. Jovanovic, "A design approach for server power supplies for networking applications," *APEC 2000. Fifteenth Annual IEEE Applied Power Electronics Conference and Exposition (Cat. No.00CH37058)*, 2000, pp. 1163-1169 vol.2, doi: 10.1109/APEC.2000.822834.

[10] D. L. Caiza, F. F. Bahamonde, S. Kouro, V. Santana, N. Müller, and A. Chub, "Sliding Mode Based Control of Dual Boost Inverter for Grid Connection," *Energies*, vol. 12, no. 22, pp. 1-15, 2019, doi: 10.3390/en12224241.

[11] B. Shakerighadi, E. Ebrahimzadeh, F. Blaabjerg, and C. L. Bak, "Large-Signal Stability Modeling for the Grid-Connected VSC Based on the Lyapunov Method," *Energies*, vol, 11, no. 10, pp. 1-16, 2018, doi: 10.3390/en11102533.

[12] B. A. M. Treviño, A. E. Aroudi, A. Cid-Pastor and L. Martinez-Salamero, "Nonlinear Control for Output Voltage Regulation of a Boost Converter With a Constant Power Load," *IEEE Transactions on Power Electronics*, vol. 34, no. 11, pp. 10381-10385, 2019, doi: 10.1109/TPEL.2019.2913570.

[13] S. Nagaraj, R. Ranihemamalini and L. Rajaji, "Design and analysis of controllers for high voltage gain DC-DC converter for PV panel," *International Journal of Power Electronics and Drive System (IJPEDS)*, vol. 11, no. 2, pp. 594-604, 2020, doi: 10.11591/ijpeds.v11.i2.pp594-604.

[14] S. Narasimha and S. R. Salkuti, "Design and operation of closed-loop triple-deck buck-boost converter with high gain soft switching," *International Journal of Power Electronics and Drive System*, vol. 11, no. 1, pp. 523-529, 2020, doi: 10.11591/ijpeds.v11.i1.pp523-529.

[15] R. Zhang and B. Hredzak, "Nonlinear Sliding Mode and Distributed Control of Battery Energy Storage and Photovoltaic Systems in AC Microgrids With Communication Delays," *IEEE Transactions on Industrial Informatics*, vol. 15, no. 9, pp. 5149-5160, 2019, doi: 10.1109/TII.2019.2896032.

[16] L. Callegaro, M. Ciobotaru, D. J. Pagano and J. E. Fletcher, "Feedback Linearization Control in Photovoltaic Module Integrated Converters," *IEEE Transactions on Power Electronics*, vol. 34, no. 7, pp. 6876-6889, 2019, doi: 10.1109/TPEL.2018.2872677.

[17] A. A. Aboushady, K. H. Ahmed, S. J. Finney and B. W. Williams, "Linearized Large Signal Modeling, Analysis, and Control Design of Phase-Controlled Series-Parallel Resonant Converters Using State Feedback," *IEEE Transactions on Power Electronics*, vol. 28, no. 8, pp. 3896-3911, 2013, doi: 10.1109/TPEL.2012.2231700.

[18] K. Noussi, A. Abouloifa, H. Katir, I. Lachkar and F. Giri, "Nonlinear control of grid-connected wind energy conversion system without mechanical variables measurements," *International Journal of Power Electronics and Drive Systems*, vol. 12, no. 2, pp. 1141-1151, 2021, doi: 10.11591/ijpeds.v12.i2.pp1141-1151.

[19] F. Wu, S. Fan and S. Luo, "Small-Signal Modeling and Closed-Loop Control of Bidirectional Buck-Boost Current-Fed Isolated DC–DC Converter," *IEEE Transactions on Industrial Electronics*, vol. 68, no. 5, pp. 4036-4045, 2021, doi: 10.1109/TIE.2020.2984448.

[20] K. Khatun, V. R. Vakacharla, A. R. Kizhakkan and A. K. Rathore, "Small-Signal Analysis and Control of Snubberless Naturally Clamped Soft-Switching Current-Fed Push–Pull DC/DC Converter," *IEEE Transactions on Industry Applications*, vol. 56, no. 4, pp. 4299-4308, 2020, doi: 10.1109/TIA.2020.2995561.

[21] M. Veerachary, "Analysis of Fourth-Order DC–DC Converters: A Flow Graph Approach," *IEEE Transactions on Industrial Electronics*, vol. 55, no. 1, pp. 133-141, 2008, doi: 10.1109/TIE.2007.907677.

[22] L. Mitra and U. K. Rout, "Optimal control of a high gain DC-DC converter," *International Journal of Power Electronics and Drive Systems*, vol. 13, no. 1, pp. 256-266, 2022, doi: 10.11591/ijpeds.v13.i1.pp256-266.

[23] A. Davoudi, J. Jatskevich, P. L. Chapman and A. Khaligh, "Averaged-Switch Modeling of Fourth-Order PWM DC–DC Converters Considering Conduction Losses in Discontinuous Mode," *IEEE Transactions on Power Electronics*, vol. 22, no. 6, pp. 2410-2415, 2007, doi: 10.1109/TPEL.2007.909270.

[24] P. Azer and A. Emadi, "Generalized State Space Average Model for Multi-Phase Interleaved Buck, Boost and Buck-Boost DC-DC Converters: Transient, Steady-State and Switching Dynamics," *IEEE Access*, vol. 8, pp. 77735-77745, 2020, doi: 10.1109/ACCESS.2020.2987277.

[25] S. Misal and M. Veerachary, "Analysis of a Fourth-Order Step-Down Converter," *IEEE Transactions on Industry Applications*, vol. 56, no. 3, pp. 2773-2787, 2020, doi: 10.1109/TIA.2020.2975500.

BIOGRAPHIES OF AUTHORS

Suriyotai Supanyapong 🆔 🔍 SC Ⓟ was born in Suratthani, Thailand. He received the B.S.Tech.Ed. degree in electrical engineering from the King Mongkut's Institute of Technology North Bangkok (KMITNB), Bangkok, Thailand, in 1993, the M.S.Tech.Ed. degree in electrical from the King Mongkut's Institute of Technology North Bangkok (KMITNB), Bangkok, in 1997, and the Ph.D. degree in vocational and technical education management from the King Mongkut's University of Technology North Bangkok (KMUTNB), in 2014. He is currently an Assistant Professor with the Department of Electrical Engineering Technology, College of Industrial Technology (CIT), KMUTNB. His research interests include renewable application in power electronics system, and innovation project power electronics field. He can be contacted at email: suriyotai.s@cit.kmutnb.ac.th.

Wachiravit Pattarapongsathit 🆔 🔍 SC Ⓟ was born in Bangkok, Thailand. He received the B.Eng. degree in power electronics technology from College of Industrial Technology (CIT), King Mongkut's University of Technology North Bangkok (KMUTNB, in 2017, where he is currently working toward the M.Eng. degree in applied electrical engineering technology, Department of Electrical Engineering Technology, College of Industrial Technology (CIT), King Mongkut's University of Technology North Bangkok (KMUTNB), in 2022. His research interests include high-frequency and high efficiency converter, simulation design and analysis renewable energy system, and power electronics application. He can be contacted at email: wachiravit.pongsa@gmail.com.

Anusak Bilsalam (Member, IEEE) was born in Nakhon Si Thammarat, Thailand. He received the B.Ind.Tech. degree in power electronics technology from the King Mongkut's Institute of Technology North Bangkok (KMITNB), Bangkok, Thailand, in 2004, the M.E. degree in electrical engineering from the King Mongkut's University of Technology Thonburi (KMUTT), Bangkok, in 2010, and the Ph.D. degree in electrical engineering from the King Mongkut's University of Technology North Bangkok (KMUTNB), in 2015. From 2013 to 2017, he was a lecturer with the Division of Energy Technology and Management, Faculty of Science, Energy and Environment, King Mongkut's University of Technology North Bangkok (Rayong campus). He is currently an Assistant Professor with the Department of Electrical Engineering Technology, College of Industrial Technology (CIT), KMUTNB. His research interests include high-frequency and efficiency switching power converter, zero voltage and zero current switching techniques in resonant converter, math model of a photovoltaic cells and renewable energy system and induction/dielectric heating application. He can be contacted at email: anusak.b@cit.kmutnb.ac.th.

Damien Guilbert (Member, IEEE) was born in Paris, France, in 1987. He received the M.Sc. degree in electrical engineering and control systems and the Ph.D. degree in electrical engineering from the University of Technology of Belfort-Montbéliard (UTBM), Belfort, France, in 2011 and 2014 respectively. Since 2016, he has been an Associate Professor with the Université de Lorraine, Nancy, France, where he is currently a Permanent Member of the Group of Research in Electrical Engineering of Nancy (GREEN) Laboratory. His current research interests include power electronics, fuel cell and electrolyzer system, modeling and emulation of polymer electrolyte membrane (PEM) electrolyzers, fault-tolerant DC/DC converters for fuel cell/photovoltaic/electrolyzer applications, fault-tolerant control for fuel cell/electrolyzer systems, and energy management of multisource systems based on renewable energy sources and hydrogen buffer storage. Dr. Guilbert was involved in the creation of the first IEEE/IAS student branch and chapter in France at UTBM. He can be contacted at email: damien.guilbert@univ-lorraine.fr.

Phatiphat Thounthong (Senior Member, IEEE) was born in Phatthalung, Thailand, on December 29, 1974. He received the B.S. and M.E. degrees in electrical engineering from King Mongkut's Institute of Technology North Bangkok (KMITNB), Bangkok, Thailand, in 1996 and 2001, respectively, the Ph.D. degree in electrical engineering from Institut National Polytechnique de Lorraine (INPL), Nancy-Lorraine, France, in 2005, and the Habilitation à Diriger la Recherche (HDR) from Université de Lorraine, Nancy-Lorraine, France in 2020. Since 2012, he has been a Full Professor in the Department of Teacher Training in Electrical Engineering, King Mongkut's University of Technology North Bangkok. He is the author of 231 scientific papers (including 21 papers in IEEE Transactions/Magazines) published in Scopus with citations0=4,746 times and h-index=34. His current research interests include power electronics, electric drives, electric vehicles, electrical devices (fuel cells, photovoltaic, wind turbine, batteries and supercapacitors, nonlinear controls and observers. He can be contacted at email: phatiphat.t@fte.kmutnb.ac.th.